RSC Advances

PAPER

View Article Online
View Journal | View Issue

Cite this: *RSC Adv.*, 2023, **13**, 9983

Three-dimensional N-doped mesoporous carbon–MXene hybrid architecture for supercapacitor applications†

Abeer Enaiet Allah *

Hierarchical heterostructures of mesoporous carbon wrapped around MXene nanolayers, which combine a porous skeleton, two-dimensional nanosheet morphology, and hybrid characteristics, have attracted research attention as electrode materials for energy storage systems. Nevertheless, it remains a significant challenge to fabricate such structures due to a lack of control of material morphology with high pore accessibility for the mesostructured carbon layers. As a proof of concept, I report a novel layer-by-layer N-doped mesoporous carbon (NMC)MXene heterostructure through the interfacial self-assembly of exfoliated MXene nanosheets and block copolymer P123/melamine–formaldehyde resin micelles with subsequent calcination treatment. The incorporation of MXene layers in the carbon matrix not only creates a spacer to inhibit the MXene sheet restacking and high specific surface area, but it also renders composites with good conductivity and additional pseudo capacitance. The as-prepared electrode with NMC and MXene exhibits outstanding electrochemical performance, with a gravimetric capacitance of 393 F g^{-1} at 1 A g^{-1} in an aqueous electrolyte and remarkable cycling stability. More importantly, the proposed synthesis strategy highlights the benefit of using MXene as a buttress for organizing mesoporous carbon in novel architectures with the potential for energy storage application.

Received 28th October 2022
Accepted 17th March 2023

DOI: 10.1039/d2ra06817f

rsc.li/rsc-advances

1. Introduction

Porous carbon materials have been widely considered as electrodes for energy storage applications due to their controllable porous structure, chemical stability, and high conductivities, which are all available at a cost that is hard to accomplish with other materials.[1,2] Among these porous carbon materials, the mesoporous carbon (MC) family is especially ubiquitous and important for supercapacitor applications due to its extraordinary structural features that can offer both large effective surface areas with abundant active sites and accessible channels for accelerating ion movement and electron transfer.[3,4] Like many other porous materials, however, MC can suffer from a low degree of crystallinity, numerous framework defects, and easy electrode surface aggregation, which would consequently retard the electron transfer conductivity and weaken electrochemical catalytic activity by diminishing the active surface area.[5–8] Tackling this drawback is considered a tedious task for obtaining improved functional materials for supercapacitor applications. Compared to ordinary mesoporous structures, the two-dimensional (2D) materials with unusual physical and chemical properties, remarkable electrical properties, and large surface-to-volume ratios, which are necessary for exposing the active sites to electrolytes, are the current research flashpoint for designing superior supercapacitor electrodes.[9–12] Although applications of 2D structured materials are mostly impeded by self-restacking and severe aggregation, especially after processing into a compressed electrode; this limits their ion-diffusion and electron transport.

Meanwhile, structural engineering is a viable solution for the modulation of 2D materials into heterostructures with tailored properties that meet specific requirements for certain energy storage applications. Such heterostructures would potentially utilize all energy capabilities by inheriting the advantages of each building block while mitigating the weakness points of each one. Therefore, it is possible to employ 2D materials as structural templates to synthesize nano hierarchical carbon material architectures with uniform distributions of MC on the backbone and segregated layered structure, which is expected to greatly facilitate their electrochemical applications.[7,13] MXenes, a recently discovered class of 2D materials made up of 2D transition metal nitrides, carbides, and carbonitrides that were delaminated from their MAX layered counterparts by chemical etching, have progressed quickly since their discovery by Gogotsi in 2011.[14] The MAX phase is a group of layered ternary nitrides and carbides with the general formula $M_{n+1}AX_n$, where M denotes an early transition metal, A denotes an element from the A-group (often, group III A or IV A), X denotes carbon (C), nitrogen (N), or both, and n denotes 1, 2, or 3. 2D

Chemistry Department, Faculty of Science, Beni-Suef University, Beni-Suef 62511, Egypt. E-mail: abeer.abdelaal@science.bsu.edu.eg

† Electronic supplementary information (ESI) available. See DOI: https://doi.org/10.1039/d2ra06817f

MXene nanomaterials can be produced by selectively extracting the A element from MAX using hydrofluoric acid (HF). Surfaces of MXene are functionalized as a result of this synthesis process, mainly by O and/or OH groups with some fluorine. These terminated MXenes are referred to as $M_{n+1}X_nT_x$, where x denotes the number of termination groups and T denotes surface termination (O, OH, or F).[15]

Thus far, the thriving family of MXenes were exploited with very good performance in various applications such as energy harvesting and storage, electromagnetic interference (EMI) shielding, sensing, optoelectronics, biomedicine, and electrocatalysis for oxygen reduction reaction (ORR), oxygen evolution reaction (OER), and hydrogen evolution reaction (HER).[16,17] The 2D MXenes family is still evolving as it attracted the attention of the scientific community due to their superb metallic conductivity, remarkable mechanical and chemical stability, good thermal conductivity, superior hydrophilic properties, and a variable surface functional group that can interact with other materials.[18–20] In addition, the contribution of the excellent conductivity of MXene in its high power density in comparison with other semiconductor-type metal oxides confers the rapid charging of storage devices.[18] But, the electrode fabrication using MXene suffers from aggregation and restacking *via* hydrogen bonding and strong van der Waals forces.[21] These forces affect the surface functional group and retard ion mobility. This reason creates the motivation for the construction of 3D structure comprising both materials mesoporous carbon and 2D material. The 3D material confers a more porous skeleton and abundant active site that can serve as excellent material for storage charges in supercapacitors.[22] Among different energy storage devices, supercapacitors can replace batteries and play an essential role in energy storage and harvesting devices especially when high power delivery is needed. Supercapacitors have higher power density, longer cycle life, and larger energy storage capacity than batteries.[23–27]

The hydrothermal approach was used by Liu and colleagues to construct orderly MC on the surface of graphene aerogel to improve the electrochemical behavior of MC. Their product achieved a capacitance of 191 F g^{-1}.[7] Furthermore, Zhilin *et al.* presented the self-assembly method for the production of an ordered mesoporous carbon/$Ti_3C_2T_x$ heterostructure interface with induced spherical composite monomicelles. Their electrode exhibited 190 F g^{-1} at 5 A g^{-1}. However, these materials only accomplish relatively limited capacitances.[28]

Based on the aforementioned aspects, we have assembled MC particles in an onion morphology on 2D MXene nanosheets. The hierarchical structure offers complementary features because (i) the high conductivity of MXene nanosheets can enhance the electron conductivity of MC, (ii) the insertion of MXene layers between the MC will provide hierarchical architectures that limit MC aggregation and have high accessibility to channel pathways for ions and electrons, and (iii) MC functions as an interlayer spacer to prevent MXene nanosheets from being restacked.

In this work, we develop an elaborate approach to preparing a three-dimensional (3D) hierarchical structure of nitrogen-doped MC (NMC) with onion morphology on the surface of 2D MXene nanosheets (hereafter referred to as NMC@MXene). The hierarchical structure formed through directed self-assembly of nitrogen-containing phenol–melamine–formaldehyde resin (PMF) micelles acting as carbon and nitrogen precursor on the surface of Pluronic P123 micelles acts as a structure-directing agent in the presence of exfoliated MXene, which acts as a 2D substrate followed by carbonization treatment. The newly designed heterostructure exhibited a high surface area (over 1000 m^2 g^{-1}) due to the effective separation of MXene layers with NMC, which is created during the hydrothermal reaction. The proposed heterostructure combines the merits of NMC with accessible nanopores, which provide continuous channels for ion diffusion, and MXene nanosheets, which guarantee high electronic conductivity. The electrochemical tests show that the NMC@MXene has a high specific capacitance, of up to 439 F g^{-1}, at a current density of 1 A g^{-1}, as well as remarkable long-term durability and good rate capability; thus, granting stable energy output for supercapacitor applications.

2. Experimental section

2.1. Chemicals

Pluronic P123 (PEG-PPG-PEG), melamine, tetramethylammonium hydroxide (TMAOH), and 5.0 wt% Nafion perfluorinated resin solution were obtained from Sigma-Aldrich. Phenol, formaldehyde (37 wt%), 0.1 M sodium hydroxide and 1 M H_2SO_4 were purchased from Nacalai Tesque, Inc. HF (45%) was purchased from Wako and MAX was purchased from 11 Technology Co., Ltd. All chemicals were analytical grade and used as received.

2.2. Preparation of onion N-doped mesoporous carbon (NMC)

Firstly, the mesostructured polymer was prepared *via* organic–organic assembly process in an aqueous solution with the assistance of triblock copolymer Pluronic P123. Phenol–melamine/formaldehyde resin (P–M/F) was added as carbon and nitrogen sources. Typically, 0.19 g of phenol and 0.095 g of melamine were dissolved in 750 μL of formaldehyde aqueous solution (37 wt%) under stirring at 60 °C, leading to a colorless transparent solution after 5 min. The aforesaid clear solution was then mixed at 70 °C for 30 min while a specific volume of 0.1 M NaOH solution was added. Afterward, 5.0 mL P123 aqueous solution (containing 0.162 g of P123) was added and the solution was stirred at 65 °C for 2 h. Subsequently, 12.5 mL of distilled water was added to the mixture and the diluted solution was kept at 65 °C for another 10 h under mild stirring. After that, 10.0 mL of the obtained solution was transferred to a Teflon liner under vigorous stirring. The pH value was adjusted to approximately nine by adding an appropriate volume of 0.1 M NaOH solution. The Teflon liners were transferred into autoclaves (volume of 100 mL) for hydrothermal reaction at 130 °C for 20 h with a ramping rate of 1 °C min^{-1}. The precipitate was obtained and centrifuged at 14 000 rpm for 5 min before being three times rinsed with water and ethanol.

After drying at 60 °C, mesostructured polymers assigned as the NMC precursor were obtained. The as-made precursor was carbonized at 900 °C for 4 h under N_2 atmosphere. The ramping rate of the calcination process was 5 °C min^{-1}. The carbonized NMC was assigned as NMC-900.

2.3. Preparation of MXene

Multilayer MXene ($Ti_3C_2T_x$) was prepared by selectively etching the Al layer from the MAX (Ti_3AlC_2). In particular, 1 g of Ti_3AlC_2 was added to 25 mL HF solution (45 wt%) and the mixture was magnetically stirred at 60 °C for 18 h. The resulting suspension was then centrifuged to separate multilayer $Ti_3C_2T_x$ particles after being rinsed with deionized water several times. Then, the resulting MXene was magnetically stirred for 18 h at room temperature in 20 mL of tetramethylammonium hydroxide (TMAOH). After diluting with deionized water, TMAOH-intercalated $Ti_3C_2T_x$ was separated by centrifugation at 5000 rpm for 3 min. The obtained precipitate was dispersed in deionized water with a weight ratio of $Ti_3C_2T_x$: water of 1 : 300. To obtain a supernatant containing delaminated $Ti_3C_2T_x$ flakes, the suspension was centrifuged at 3000 rpm for 1 h after being sonicated for 2 h under flowing nitrogen (N_2). Few-layer $Ti_3C_2T_x$ was produced by filtering the decanted supernatant and vacuum-drying it.

2.4. Preparation of NMC@MXene

The NMC@MXene was prepared by the same described previous method for preparation of NMC but after the addition of the water, 10 mL of $Ti_3C_2T_x$ MXene solution was added drop by drop under continuous stirring. Then, proceeding the hydrothermal process and calcination treatment as described previously in Section 2.2. By changing the amount of $Ti_3C_2T_x$ from 10 to 20 and 30 mL, samples NMC@MXene-10, NMC@MXene-20, and NMC@MXene-30, respectively, were obtained.

2.5. Preparation of NMC/MXene

Aqueous dispersions of 20 mg MXene nanosheets in 5 mL water and 40 mg of the prepared polymer of NMC particles in 10 mL water were mixed under sonication for 2 h. The mixed dispersions were vacuum filtered using Celgard 3501 membranes and then vacuum dried at 80 °C for 6 h. The prepared sample was carbonized at 900 °C for 4 h under an atmosphere of N_2. The calcination process ramped up at a rate of 5 °C min^{-1}. The carbonized sample is hereafter referred to as NMC/MXene.

2.6. Characterization

The morphological details of the samples were captured by a field emission scanning electron microscope (SEM, HITACHI SU-8230) operating at 5.0 kV and a transmission electron microscope (TEM, JEOL JEM-2100F) operated at 200 kV was employed to investigate the inner mesoporous structure. Small-angle X-ray scattering (Rigaku NANO-Viewer) equipped with a camera length of 700 mm was used to evaluate the pore-to-pore distance with Cu Kα radiation (40 kV, 30 mA). The phase composition of the samples was checked by wide-angle X-ray X diffraction (XRD) of Rigaku RINT 2000X diffractometer with monochromated Cu-Kα radiation ($\lambda = 1.54$ Å) (40 kV, 40 mA) at a scanning rate of 1° min^{-1}. The textural properties of the samples were analyzed by nitrogen (N_2) adsorption–desorption measurements at 77 K with the specific surface area (SSA) determined based on the Brunauer–Emmett–Teller (BET) theory in the relative pressure range of 0.05–0.3. Pore size distribution data were obtained from the N_2 adsorption–desorption isotherms, according to the non-local density functional theory (NLDFT) method. Each sample had a vacuum degassing process at 120 °C for 16 h before the BET measurement. The chemical state of nitrogen was investigated by using X-ray photoelectron spectroscopy (PHI Quantera SXM) with Al Kα radiation (20 kV, 5 mA). The shift of binding energy was calibrated using the C 1s level at 284.5 eV. The thermal stability of samples was assessed with thermogravimetric analysis (6300 TG/DTA, Hitachi HT-Seiko Instrument Exter) under air heating from room temperature to 850 °C at 5 °C min^{-1}.

2.7. Electrochemical measurements

The as-prepared NMC-900, MXene, NMC@MXene-*x*, and NMC/MXene were ground before preparing the inks. In a typical experiment, 2.0 mg of sample was dissolved in 400 μL of 1 : 2 (v/v) isopropanol/water mixture solvent (containing 20 μL of 5.0 wt% Nafion solution) and sonicated for at least 30 min to form a homogenous ink. After that, 200 μL of the suspension was dropped onto the flexible graphite paper (working electrode) with an area of 1 × 1 cm^2, and thickness of 1 mm and dried at 60 °C. The mass loading was 1.0 mg cm^{-2} and the thickness of the electrode film was measured to be around 15–25 μm. In addition, I choose flexible graphite paper as the current collector because of its excellent electrical conductivity as well as its negligible capacitive performance (usually below 1 F g^{-1}), which would contribute little to the total capacitance of the prepared working electrode. All electrochemical measurements were carried out on a CHI 660E instrument. In a three-electrode system, the electrochemical performances of working electrodes were investigated by cyclic voltammetry (CV) and galvanostatic charge–discharge (GCD) in 3 M KOH, with a platinum wire as the counter electrode and saturated calomel electrode as the reference electrode. The specific capacitance for as-made electrodes was calculated from the GCD curves. The test of long-term stability for NMC@MXene-30 was conducted by cycling between 0.0 and −1.0 V *vs.* Ag/AgCl in 3 M KOH at a scan rate of 100 mV s^{-1}. In general, the gravimetric specific capacitance (C_m, F g^{-1}) was calculated using the following equation:

$$C_m = \frac{I \times t}{m \times \Delta V} \quad (1)$$

where I is the discharge current (A), t is the discharge time (s), m is the mass of active material (g), and ΔV is the potential change during the discharge process (V).

The volumetric capacitance (C_v) was calculated according to the following equation:

$$C_v = \rho C_m.$$

ρ was measured by dropping the ink on the aluminum foil, which was followed by drying and pressing, and then calculated according to the following formula: $\rho = m/Sd$, where m is the mass of the dried film of NMC@MXene ink (g), which was coated on an aluminum foil. S is the area of the film (cm^{-2}) and d is the thickness (cm).

3. Results and discussion

Fig. 1 provides schematic illustrations and transmission electron microscopy (TEM) images of the NMC@MXene heterostructure synthesis procedure. A homogenous solution containing PMF/P123 resol micelles, which provide subunit building blocks rich in phenolic hydroxyl groups, is initially prepared in the presence of NaOH and according to the organic self-assembly process (Fig. 1a). Subsequently, the solution is mixed with the MXene suspension obtained by etching Ti_3AlC_2 while stirring for 30 min. This suspension is used as a substrate for organizing layers of close-packed PMF/P123 composite micelles. The surface functional groups of the MXene material can be strongly interacted with *via* hydrogen bonding between the –OH of PMF/P123 composite micelles (Fig. 1b). The PMF/P123@MXene heterostructure is created through hydrothermal treatment at 130 °C for 20 h; subsequent polymerization of the PMF/P123 micelles causes them to wrap closely around and between MXene layers. MXene flakes have a greater attractive interaction with the PMF/P123 surface than that between PMF/P123 monomicelles, which is the pivotal issue for assembly (Fig. 1c). Finally, a follow-up calcination treatment under a nitrogen atmosphere is carried out to convert the resin network of PMF/P123–MXene to NMC@MXene. The obtained hierarchical heterostructure materials show a multilayer sandwich-like structure (Fig. 1d).

FESEM and TEM images illustrate the detailed microstructure and morphology of the as-synthesized materials. As shown in Fig. 2a, the 2D multilayers and clean, crumpled surface of exfoliated MXene flakes illustrate that the Al layers were selectively etched and formed $Ti_3C_2T_x$ plates in good accordance with previously reported data.[20] Therefore, the plates can be used as a substrate for the gradual growth of PMF/P123 monomicelles on their surface and the formation of a heterostructure composite. From the SEM images (Fig. S1a†), homogenous spherical particles of the as-prepared polymer formed with good morphological retention and diameters ranging from 80 to 100 nm in NMC after calcination (Fig. 1b). Concurrently, from the SEM and TEM observations in Fig. 2b, c and S1b,† the onion structure with a highly developed porous structure is evidenced by the internal tubular mesochannels running in a circular track within each particle. This structure can act as a diffusion channel for the electrolytes. High-angle annular dark-field scanning TEM (HAADF-STEM) images confirm the onion-like morphology with uniform distributions of carbon, nitrogen, and oxygen (Fig. S1c–f†). A typical SEM image (Fig. 2d and e) reveals that the as-prepared P123/PMF@MXene-10 polymer displays a 3D hierarchically tiered structure with a rough surface. In this structure, the $Ti_3C_2T_x$ MXene is fully covered by layers of NMC. The electrostatic self-assembly of positively charged NMC with negatively charged

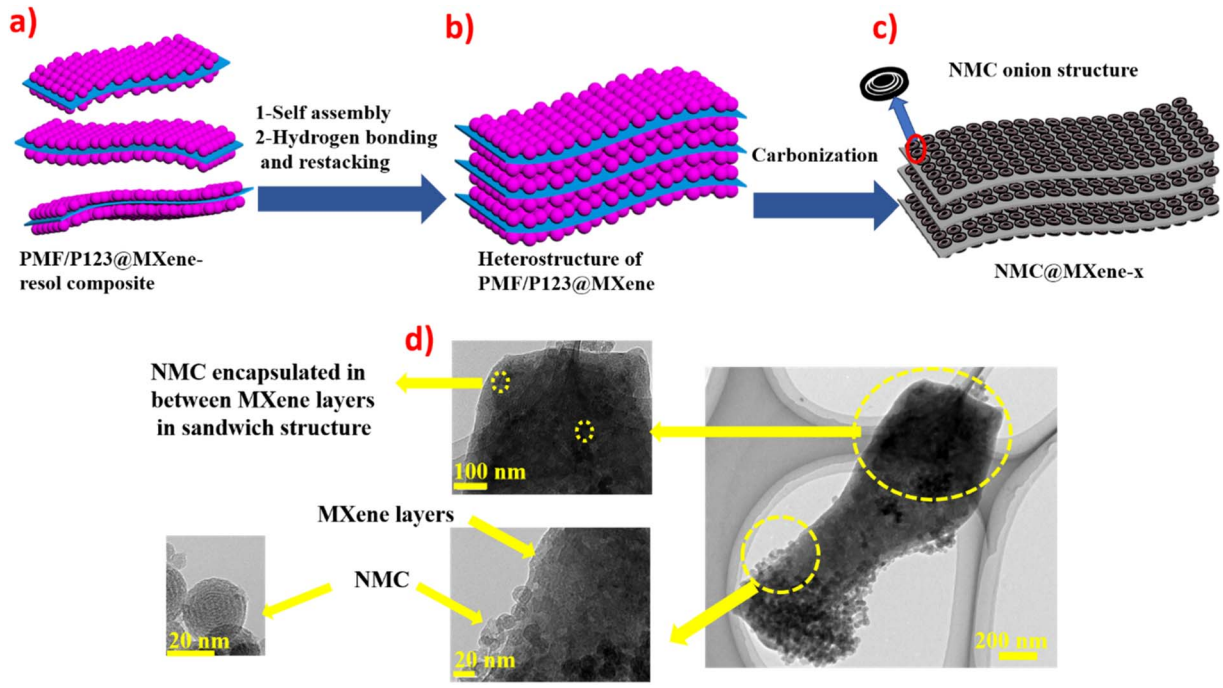

Fig. 1 Hierarchical NMC@MXene heterostructure formation process: (a) self-assembly of PMF/P123 micelles on MXene surface *via* hydrogen bonding, (b) formation of PMF/P123@MXene heterostructure by restacking and further assembly, and (c) formation of NMC@MXene after carbonization. (d) TEM for NMC@MXene where NMC is encapsulated between MXene layers.

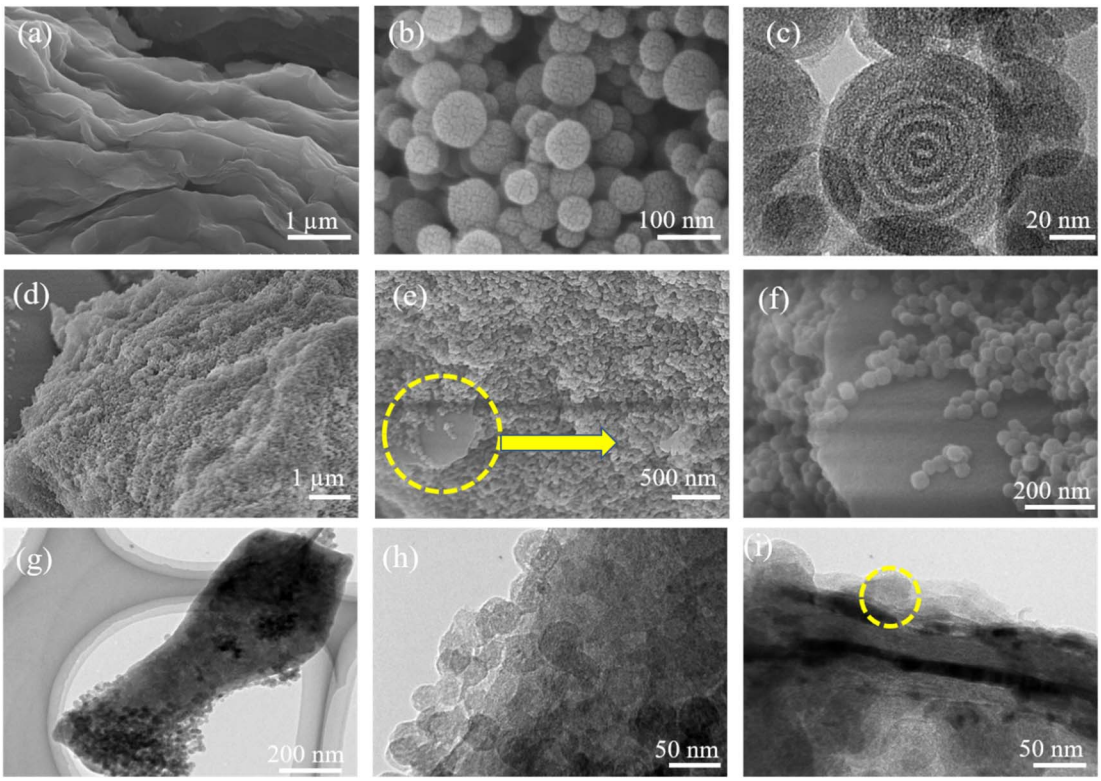

Fig. 2 (a) SEM images of the as-prepared MXene; (b and c) SEM and TEM images of NMC-900; (d) SEM image of as-prepared NMC@MXene-10; (e and f) SEM images of calcinated NMC@MXene-10; (g–i) TEM images of calcinated NMC@MXene-10.

MXene layers is considered to be the main strategy for stabilizing the structure in the form of tiered alternating layers to minimize the self-restacking of MXene. Closer observation of the P123/PMF@MXene nanosheet at higher magnification (Fig. 2f) indicates successful stacking between the MXene surface and the NMC (yellow circle). Further confirmation that the NMC@MXene-*x* hybrid maintains its morphology without any obvious distortion, even after calcination, is shown in Fig. S2a–d.† As can be seen in Fig. 2g–i and S3a, b,† TEM and high-resolution TEM (HRTEM) observations confirm results indicating successful deposition, intercalation, and embedding of NMC on the MXene surface and in between its layers. Obviously, when increasing the dosage of MXene, its lamellar 2D nanosheet structures become more discernible and provide more positions for NMC micelles to deposit and arrange by crosslinking in a thicker hierarchical tiered structure due to the formation of multilayers between NMC and MXene. This effectively prevents NMC aggregation, and MXene restacking (Fig. S2a–d†), and increases the specific surface area for enhanced electrochemical properties.

In addition, TEM and HRTEM of calcinated NMC@MXene-30 confirm that MXene retains its 2D flake-like morphology in the presence of NMC, even after annealing at 900 °C (Fig. 3a and b). However, HRTEM of the MXene layer at high magnification (Fig. 3c) presents 0.35 nm lattice spacing corresponding to anatase TiO_2 nanocrystals, which have been found to nucleate on the NMC@MXene surface during the calcination process.[29–31] This result is also supported by the selected area electron diffraction (SAED) pattern presented in Fig. 3d, which consists of two phases: anatase TiO_2, which is evidenced by the appearance of the diffraction ring, and retained MXene phase, which is verified by the hexagonal symmetry as well as that of parent-phase Ti_2AlC_2.[14,30,32]

Importantly, the HAADF-STEM measurements of NMC@MXene-30 were performed to further probe the uniform distribution of MXene layers within the NMC skeleton and to confirm the successful intercalation of NMC with MXene layers (Fig. S4†). As can be observed in the HAADF-STEM elemental mappings, N and C elements are evenly dispersed on the MXene sheets, confirming the effective intercalation of NMC on the MXene surface.

In light of the previous structure's description, the electrostatic self-assembly strategy results in the formation of a hierarchical layered structure with increased interlayer spacing. This structure is more accessible for electron transfer between NMC and MXene nanosheets and is favorable for the transport of electrolyte ions during rapid charge/discharge processes.

It is noteworthy that the SEM, TEM, HRTEM, and HAADF-STEM observations in Fig. 4 for the mixed NMC/MXene sample, which was prepared by simply mixing MXene and NMC ultrasonically, displayed a lamellar tiered structure with an even distribution of Ti, C, N, and O (*via* elemental mapping images). This further confirms the successful interpolation of NMC particles in a continuous MXene network with an open structure to ease electron transfer and ion transport.

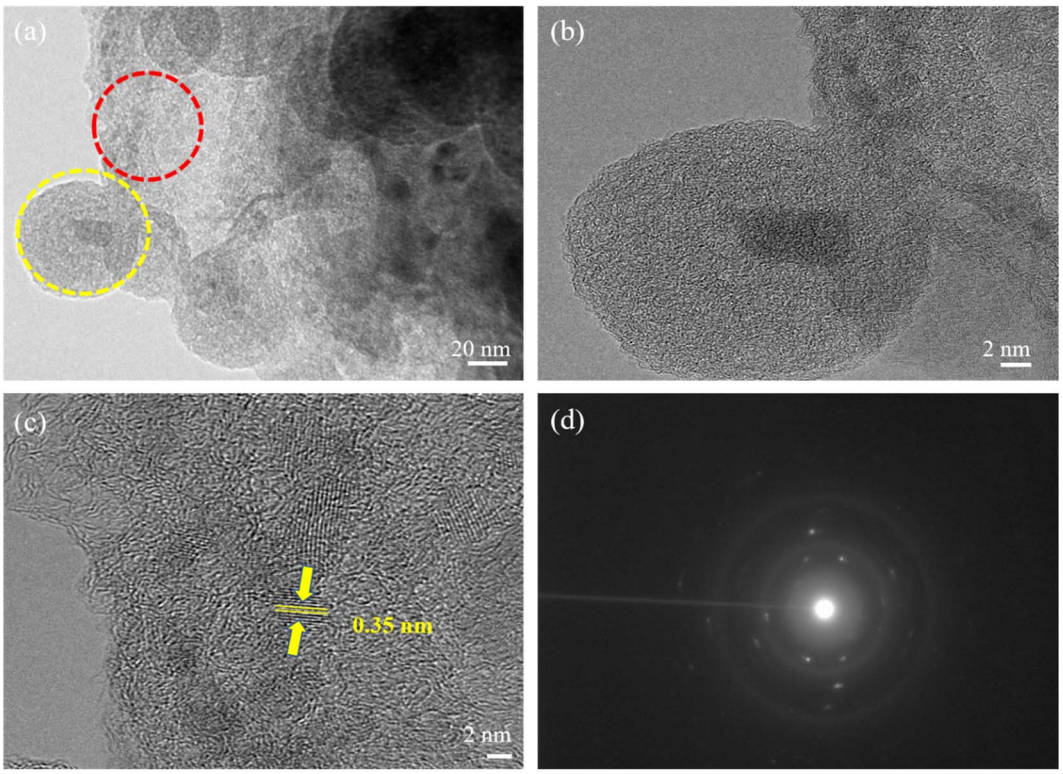

Fig. 3 (a) TEM, (b) HRTEM, [yellow circle area in (a)], and (c) HRTEM [red circle area in (a)] images, and (d) SAED pattern of calcinated NMC@MXene-30.

X-ray diffraction (XRD) measurements were obtained to characterize the prepared samples and confirm the intercalation process between MXene and NMC. As shown in Fig. 5a and S5a,† the pristine MXene displays clear diffraction peaks at 6°, 18.1°, and 60.6°, which correspond to (002), (004), and (110) planes, respectively. In addition, some (00*l*) peaks can be clearly observed in the inset of Fig. S5† and these are typical peaks corresponding to $Ti_3C_2T_x$.[14] Moreover, some weak peaks appear at 25°, 38°, 47.9°, 54°, and 62° which indicates partial oxidation of Ti atoms during calcination even under inert N_2 gas atmosphere and formation of anatase TiO_2 due to the presence of some oxygen molecules in the reaction chamber.[28,29] NMC displays two characteristic peaks at 22° and 44°, which can be attributed to the (002) and (101) crystallographic planes of graphitic carbon, respectively.[33,34] After insertion of the MXene between the NMC, and the carbonization in NMC@MXene-*x* and NMC/MXene, the main diffraction peaks of MXene at (002) disappeared, which confirms the total encapsulation of NMC as an interlayer spacer between MXene layers and the efficient inhibition of MXene restacking.[35,36] Furthermore, the XRD patterns of NMC@MXene-*x* display identical remaining peaks for pristine NMC and without titanium oxide peaks, which confirms that the inherent structure is well preserved after the calcination treatment. Simultaneously, the MXene peaks become unclear, which is consistent with the XRD results of other MXene-carbon composites.[37]

In contrast, the physically mixed NMC/MXene displays nearly identical peaks for pristine MXene and NMC. These results are further proven by small-angle X-ray scattering (SAXS) data.

The NMC and NMC@MXene-*x* SAXS patterns in Fig. S5† and 5b show well-resolved scattering peaks at $2\theta = 1.1°$, which indicates the highly periodic internal mesoporous structure of the NMC layer structure.[38] On the contrary, this peak appears weak in NMC/MXene sample, which may be due to the shielding effect caused by MXene on the surface of NMC. Nitrogen adsorption–desorption isotherm measurements were conducted to study the surface area and porosity change when adding different amounts of MXene. As shown in Fig. S5c† and 5c, NMC, NMC@MXene-*x*, and NMC/MXene samples display typical type-IV hysteresis loops, which are caused by the capillary condensation of N_2 inside the mesopores. Clearly, the steep N_2 adsorption at a low relative pressure ($P/P_0 < 0.1$) is considered evidence of the formation of micropores within the mesopore walls during carbonization. Obviously, the pristine MXene displayed a low surface area of 298.52 $m^2\ g^{-1}$ with a small pore volume of 0.61 $cm^3\ g^{-1}$ due to natural restacking. Interestingly, increasing the amount of added MXene results in greater surface areas and larger pore volumes, as listed in Table 1. Compared to the surface area of host material NMC (648.972 $m^2\ g^{-1}$), NMC@MXene-10 had a surface area of 783.857 $m^2\ g^{-1}$, which increased to 818.824 $m^2\ g^{-1}$ in NMC@MXene-20 and 1020 $m^2\ g^{-1}$ in NMC@MXene-30. Even the physical mixed

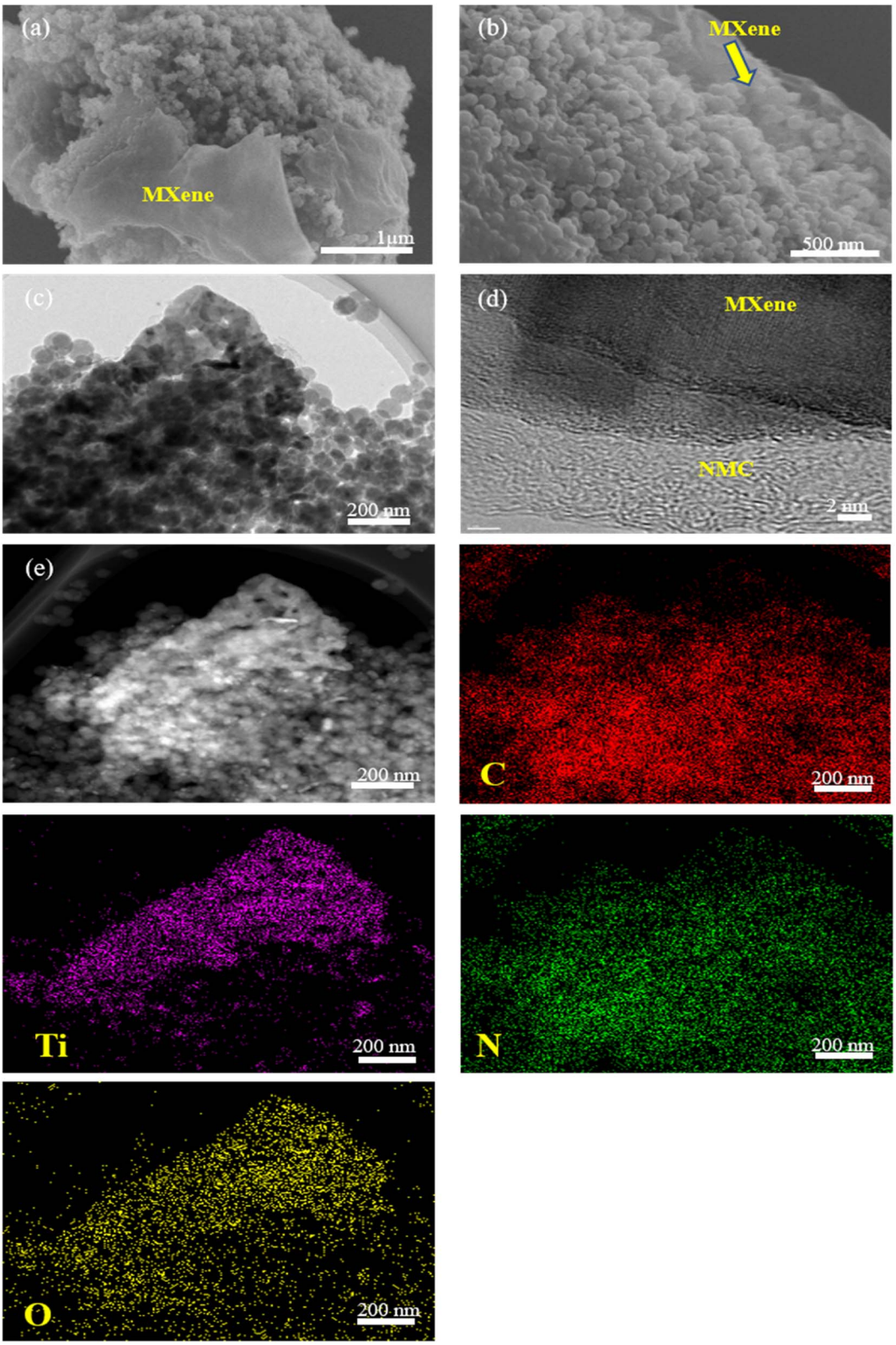

Fig. 4 (a and b) SEM, (c) TEM, (d) HRTEM images, and (e) HAADF-STEM image with elemental mappings of NMC/MXene.

hybrid NMC/MXene showed an increased surface area (703.745 $m^2\ g^{-1}$) compared to the host material NMC. These results indicate that MXene is the most important factor for improving porosity and enhancing surface area in favor of creating more active sites for electron transfer and available transportation bridges for ion diffusion. The role of MXene depends on

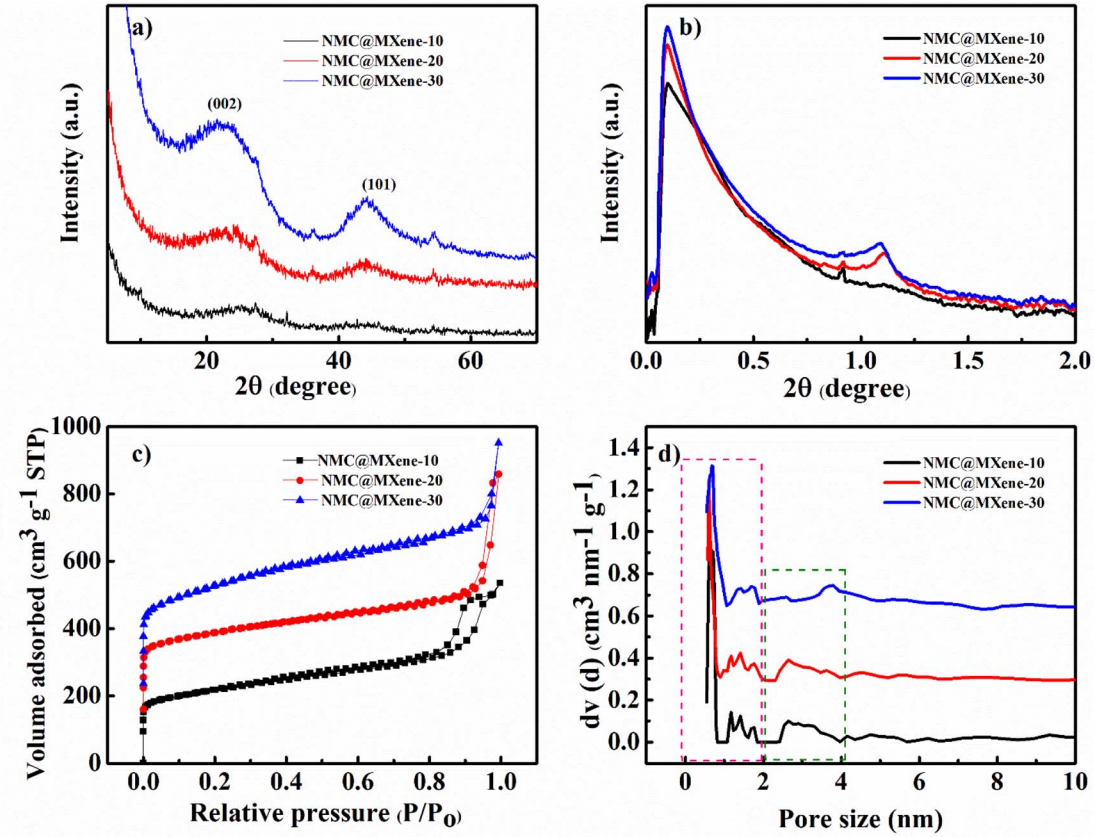

Fig. 5 (a) XRD and (b) SAXS patterns, (c) N_2 adsorption–desorption isotherms, and (d) the pore size distribution of NMC@MXene-*x* (*x* = 10, 20, and 30).

Table 1 Physiochemical properties of NMC, MXene, NMC@MXene-*x*, and MXene/NMC

Sample	SSA ($m^2\ g^{-1}$)	S_{micro} ($m^2\ g^{-1}$)	V_{pore} ($cm^3\ g^{-1}$)
NMC	648.972	256.996	1.10
MXene	298.52		0.60
NMC@MXene-10	783.857	403.849	0.82
NMC@MXene-20	818.824	383.390	1.08
NMC@MXene-30	1015	270.25	1.0
MXene/NMC	703.745	487.140	0.95

impeding NMC agglomeration by its insertion between the NMC onion structure in the hierarchical structure, resulting in a much higher available surface area and mesopores.

The pore size distribution was calculated from the adsorption branch. Fig. 5d and S5d† reveal the presence of pores with diameters of 0.6 nm and 1.4 nm (micropore range, <2 nm), and 2.5 nm (mesopore range) in the NMC@MXene-*x* and NMC/MXene, which is the same as that of NMC. These results confirm that the insertion of MXene layers does not affect the innate NMC structure. The prepared samples were further examined by Raman analysis. MXene displayed characteristic peaks around 201 400, and 640 cm^{-1}, which correspond to pristine $Ti_3C_2T_x$.[39] All samples display two strong peaks around 1350 cm^{-1} and 1591 cm^{-1} that can be matched to disordered sp^3 generated by edges and defects in the carbon lattice (D band) and graphitic sp^2 carbon (G band), respectively (Fig. S6†). The intensity ratio of the D and G bands (I_D/I_G values) can be used to measure the ordering level and degree of graphitization of carbon samples. As shown in Fig. S6,† NMC, and pristine MXene manifested the highest I_D/I_G value of 0.99 compared to 0.987 for NMC@MXene-10, 0.965 for NMC@MXene-20, 0.966 for NMC@MXene-30, and 0.972 for NMC/MXene. These results confirm that the insertion of MXene layers leads to the formation of a highly graphitic framework. Notably, I_D/I_G decreases with the increasing amount of MXene in the hybrid, which confirms the role of MXene in forming defect-free structures.

To further confirm MXene encapsulation in the NMC@MXene-30 hybrid structure and to check the surface electronic states and the chemical composition after calcination under a nitrogen atmosphere, X-ray photoelectron spectroscopy (XPS) measurements were collected. As shown in Fig. 6a and S7,† the high-resolution XPS of the Ti 2p core level of MXene can be fitted with four doublets (Ti $2p_{3/2}$–Ti $2p_{1/2}$) with a fixed area ratio equal to 2 : 1 and a doublet separation of 5.7 eV. The peaks located at 456.8 and 462.8 eV correspond to the $2p_{3/2}$ and $2p_{1/2}$ orbits of Ti^{3+} in $Ti_3C_2T_x$ MXene, respectively.[40] Signals at 459 and 465 eV can be ascribed to the $2p_{3/2}$ and $2p_{1/2}$ doublet of Ti^{2+}, respectively, which indicate that titanium is partially oxidized under high-temperature calcination (TiO_2 formation was detected by wide-angle XRD, as shown in Fig. S5†,[19,31,41] after the

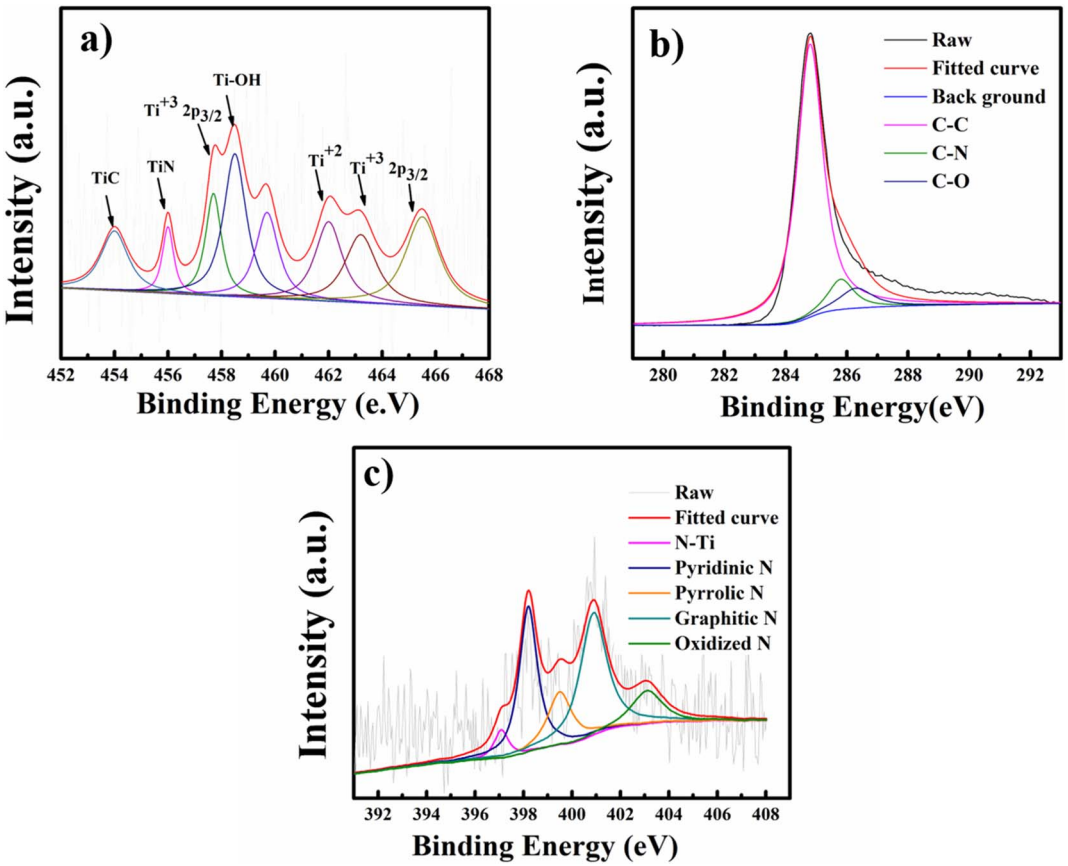

Fig. 6 High-resolution XPS spectra of (a) Ti 2p, (b) C 1s, (c) N 1s of NMC@MXene 30.

formation of composites with different percentages of MXene). The peak at 456.3 eV is ascribed to the presence of Ti–N bonds due to covalent bonding formation between MXene and NMC.[42] Clearly, the resulting NMC@MXene displays decreased intensity for the TiO_2 peak at 459 eV and increased intensity for the TiC peak at 454 eV. This confirms that the existence of NMC around the MXene layers leads to an inert condition that prevents the oxidation of MXene at high temperatures.[41] The peak at 458.5 eV belongs to Ti–OH.[40,43] Furthermore, to determine the origin of the big difference between pristine MXene and its hybrid after combining with NMC, the shift of the Ti 2p profile of NMC@MXene-*x* to a higher binding energy region compared to that of pure MXene is investigated. For example, the Ti^{4+} peak shifts from 459.0 to 459.7 eV in NMC@MXene-*x* (Fig. S7†). This reveals that the interaction of NMC with Ti weakens the Ti atom electron density, which can increase material conductivity for supercapacitor applications.[41,44]

The XPS spectrum for C 1s of NMC@MXene-*x* demonstrates three peaks at 284.8, 285.7, and 287.2 eV corresponding to C–C, C–N, and C–O signals, respectively (Fig. 6b and S8†). These results are in good agreement with the XPS of NMC and MXene, and confirm nitrogen doping in the carbon matrix.[39,42] It is noteworthy that the missing C–Ti signal in MXene can be attributed to the partial oxidation of its surface at high temperatures and the formation of TiO_2. The disappearance of this signal in the composite is due to the effect of NMC, which covers the entire surface of $Ti_3C_2T_x$ MXene,[44] and to the removal of C–Ti–O_x during nitrogen doping.[39]

The N 1s spectrum of NMC in Fig. 6c and S9† is deconvoluted into four peaks at 398.2, 399.5400.9, and 403.1 eV, which correspond to pyridinic N, pyrrolic N, graphitic N, and oxidized N, respectively.[45] The N_2 spectrum for NMC@MXene-*x* displays the same peaks as NMC and demonstrates a difference with an extra fifth peak located at 397.09 eV and corresponding to Ti–N, which confirms the successful doping of N into the MXene matrix. The two highest nitrogen-content species in NMC@MXene-*x* are graphitic and pyridinic.[46] The high percentage of graphitic carbon is a result of the high annealing temperature.[47] The pyridinic N confers a pair of electrons for conjugation with the π-conjugated rings, as a result, it can provide the NMC@MXene-*x* electron donor characteristics and increase the capacitance.[40,42]

The thermal stability of the MXene hybrid was measured using thermogravimetric analysis (TGA) under the flow of nitrogen (Fig. S10†). Pristine MXene and NMC were also measured for comparison. As can be seen in the figure, the mass decreases of the MXene can be divided into two stages. The first stage of heat treatment (room temperature to 450 °C) is mass loss due to the loss of physically adsorbed water or gases, such as O_2, from the MXene interlayers. The mass loss between 450 and 900 °C is caused by the removal of the remaining isolated OH groups and the chemically adsorbed functional groups

bonded to the surface. In Fig. S10,† the overall weight loss of MXene (33 wt%) at 850 °C, which is negligible relative to the NMC (95 wt%), reveals that MXene possesses greater thermal stability than NMC.

Moreover, the mass loss in the thermogravimetric analysis curve of NMC@MXene-*x* ($x = 10$, 20, and 30) can be divided into three distinct stages. In the temperature range of 25–200 °C, a small amount of weight loss (3.3%) is due to either the evaporation of adsorbed water or gaseous substances on the surface of the powder material. The second weak weight loss, from 200 °C to 450 °C, is attributed to the decomposition of chemically adsorbed functional groups.[48] The last stage displays swift weight loss at a temperature range of 450–550 °C, which is likely derived from the degradation of the NMC skeleton construction.[42]

Considering the unique structural advantages of NMC, as well as its insertion into the MXene layers, the resultant hybrids with high surface area, N doping, high conductivity, and alternated layer structure are expected to be indispensable for achieving large gravimetric capacitance, high stability, and rate capability supercapacitor applications. The electrochemical performance of NMC/MXene, NMC@MXene-*x* with pristine MXene, and NMC were investigated using a three-electrode system, with 3 M KOH as the electrolyte to reveal the synergistic effect between MXene and NMC as supercapacitor electrodes.

As shown in Fig. 7a, the cyclic voltammetry (CV) curve at 5 mV s^{-1} displays a rectangular curve with a pair of redox peaks that include cathodic peaks at about −0.8 V and anodic peaks at around −0.7 V. These reveal that the capacitance mainly resulted from the combination of electric double-layer charge storage of carbon material with pseudo capacitance associated with the partial change of the Ti oxidation state.[49] The CV curves in Fig. 7a for all hybrid samples, including NMC/MXene and NMC@MXene-*x*, obviously display a higher current, larger integral area, and a larger capacitance than that of pure MXene and NMC, which indicates capacitance improvement. Remarkably, NMC@MXene-30 demonstrated the highest augmentation in the CV integration area, showing its better electrochemical properties. At a high scan rate of 500 mV s^{-1}, the CV curve of

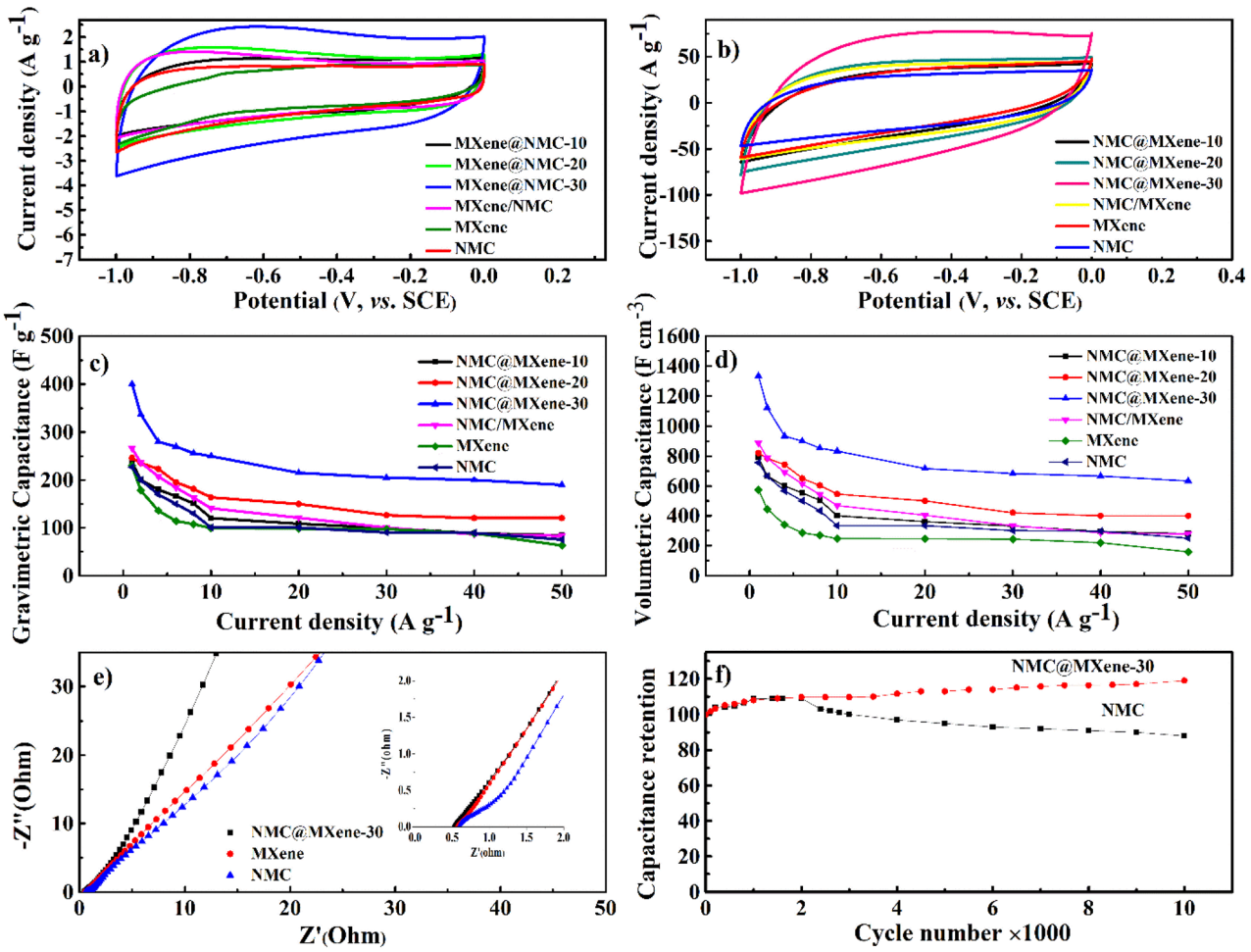

Fig. 7 Electrochemical performance of NMC@MXene-*x* ($x = 10$, 20, and 30), MXene, and NMC tested in a three-electrode system. CV curves at scan rates of (a) 5 and (b) 500 mV s^{-1}; plots of (c) C_m and (d) C_v *versus* different current densities for NMC@MXene-*x* ($x = 10$, 20, and 30), MXene, and NMC; (e) Nyquist plots of NMC@MXene-30, MXene, and NMC (with an enlarged view of the high-frequency regime), and (f) cycling stability performance of NMC@MXene-30 and NMC at a scan rate of 100 mV s^{-1}.

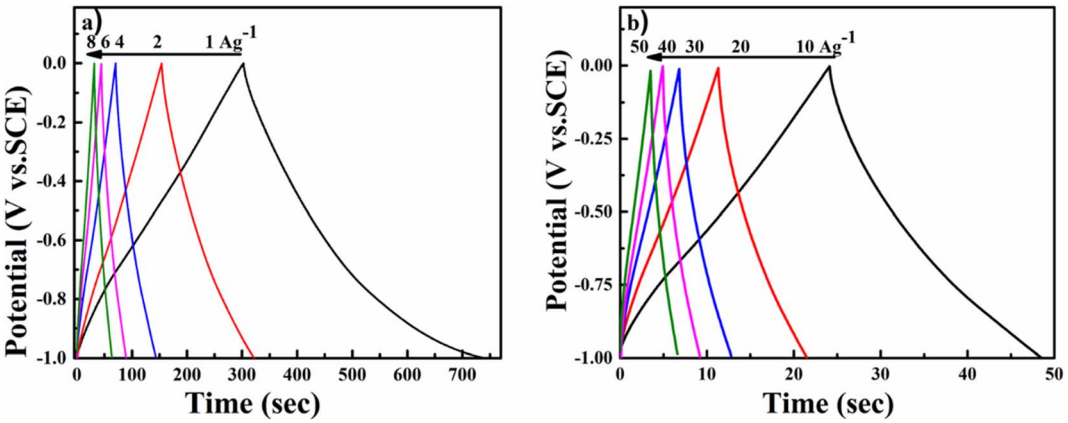

Fig. 8 Charge discharge curve of NMC@MXene-30.

NMC@MXene-30 still maintains a well-shaped rectangular curve compared to NMC and MXene (Fig. 7b). This data indicates the highly capacitive performance and excellent rate capability of NMC@MXene-30 due to ion-accessible pathways. The galvanostatic charge/discharge (GCD) curves at different current densities for all sample electrodes display roughly triangle shapes in Fig. 8 and (Fig. S11–S15†). This confirms the high-capacitive reversibility of NMC with a MXene-based supercapacitor.[50,51]

As shown in Fig. 7c the gravimetric capacitances at 1 A g^{-1} were calculated based on the GCD for NMC@MXene-30, NMC@MXene-20, NMC@MXene-10, and NMC/MXene, which were 393, 247, 236, and 266 F g^{-1}, respectively. The capacitances of MXene and NMC were 230 and 227 F g^{-1}, respectively. Upon increasing the current density, NMC@MXene-30 displayed a capacitance as high as 233 F g^{-1} can be retained at 50 A g^{-1}, corresponding to capacitance retention of 60%. For comparison, the capacitance retention of NMC@MXene-20, NMC@MXene-10, NMC/MXene, MXene, and NMC at 50 A g^{-1} were 51%, 35%, 31%, 28%, and 27%, respectively. Remarkably, NMC@MXene-30 achieved higher capacitance than previously reported NMC/MXene electrodes, as shown in Table 2.[20,52–57] Accordingly, capacitance enhancement of the NMC@MXene-30 electrode is mainly attributed to extra MXene, which induces a greater arrangement of NMC in the form of porous tiered layers to provide more accessible mesopores and tunnels for facilitating ion transport over the entire surface area while maintaining its conductivity. More importantly, increasing the interlayer space of MXene effectively mitigates its nanosheet restacking and exposes more Ti atoms to participate in the redox reaction. Therefore, the insertion of MXene pseudo capacitance accelerates rapid ion intercalation/deintercalation into the NMC tunnels and layered material, which supplies additional capacitive properties.[20,58]

In addition, the volumetric capacitance was calculated for all electrode samples at various current densities (Fig. 7d). The volumetric capacitance for NMC@MXene-30 at 1 A g^{-1} was calculated to be 1300 F cm^{-3}, which is far surpassing those of NMC@MXene-20 (820 F cm^{-3}), NMC@MXene-10 (790 F cm^{-3}), NMC/MXene (887 F cm^{-3}), MXene (575 F cm^{-3}), NMC (757 F cm^{-3}), and other previously published NMC/MXene-based electrodes (Table 2).[20,52,56,59–61]

Electrochemical impedance spectroscopy measurements were conducted in the frequency range from 10^{-2} to 10^{5} Hz to comprehend the improved capacitance and the kinetics of electron transfer and ion transport in the NMC@MXene-30, MXene, and NMC electrodes (Fig. 7e). In the high-frequency region, NMC exhibited the largest semicircle, indicating that it had a larger equivalent series resistance (ESR) with higher charge-transfer resistance than the NMC@MXene-30 and MXene. In the low-frequency region, NMC@MXene-30 displays a much steeper gradient curve than that of NMC and MXene, implying that the NMC@MXene-30 sample has the best ion-diffusion capability.[62]

Moreover, the long-term cycling stability of the NMC@MXene-30 and NMC electrodes was investigated by repeating a typical CV test at 100 mV s^{-1} for 10 000 cycles (Fig. 7f). The NMC electrode retains 88% of the initial capacitance after 10 000 cycles. The capacitance retention in NMC@MXene-30 increases gradually until achieving 105%. This result can be ascribed to the activation of material by improved wetting *via* ion intercalation/deintercalation into the microchannels in the hierarchical layered structures. At first cycles, the initial activation of electrode surface area by electrolyte wettability and thereby better access and migration of the ions into the micropores, mesopores, and mesochannels of the material with increasing CV cycles, so improving the cycling capacity.[33,63,64]

To evaluate the usability of NMC@MXene-30 for supercapacitors, its electrochemical behavior was measured in a two-electrode system using 3 M KOH as the electrolyte. Fig. 9a presents CV curves in a voltage window ranging from −1 to 0 V of the symmetrical NMC@MXene-30 supercapacitor. The CV curves of NMC@MXene-30 maintain an ideal quasi-rectangular shape, even at high scan rates of 500 mV s^{-1}, which further confirms its good rate capability and excellent rate performance.[65] In addition, close observation at 1, 3, 5, and 10 mV s^{-1} for NMC@MXene-30 reveals the rectangular-like shape implying ideal capacitive behavior (Fig. S16†). The galvanostatic charge curves with their symmetric counterpart of the discharge

Table 2 Summary of, gravimetric and volumetric performances of previously reported MXene-based electrodes tested with the three-electrode system in aqueous electrolytes

Electrode	Scan rate/current density	C_m/F g^{-1}	C_v/F cm^{-3}	Electrolyte	Ref.
$Ti_3C_2T_x$/RGO	2 mV s^{-1}	—	435	1 M $MgSO_4$	59
	200 mV s^{-1}	—	320		
Sandwich-like $Ti_3C_2T_x$/SWCNT	2 mV s^{-1}	—	390		
	200 mV s^{-1}	—	280		
Sandwich-like $Ti_3C_2T_x$/MWCNT (paper electrode)	2 mV s^{-1}	150	321		
	200 mV s^{-1}	117	250		
Pure MXene	2 mV s^{-1}	303	1000	3 M H_2SO_4	20
MX-rHGO_3	2 mV s^{-1}	438	1445		
	500 mV s^{-1}	302	997		
MXene hydrogel	2 mV s^{-1}	380	1500	1 M MgSO4	52
PPy/$Ti_3C_2T_x$	5 mV s^{-1}	—	1000	1 M H_2SO_4	60
$Ti_3C_2T_x$	2 mV s^{-1}	120	—	1 M H_2SO_4	53
MXene/CNF	300 mV s^{-1}	90			
MXene/AuNPs	5 mV s^{-1}	278	—	1 M H_2SO_4	54
	—				
Carbonized PAN/$Ti_3C_2T_x$ electrospun fibers	10 mV s^{-1}	88		1 M H_2SO_4	55
$Ti_3C_2T_x$	1 A g^{-1}	83	464	1 M H_2SO_4	56
$Ti_3C_2T_x$/RGO	1 A g^{-1}	116	361		
MXene/aromatic poly(ether amide) (PEA)-derived hybrid CNFs (HCNFs)	1 A g^{-1}	350			57
	10 A g^{-1}	190			
NOMC	1 A g^{-1}	—	420		61
	20 A g^{-1}	—	258		
NMC@MXene-30	**1 A g^{-1}**	**393**	**1300**	**3 M KOH**	**This work**
	50 A g^{-1}	**190**	**634**		
NMC@MXene-20	1 A g^{-1}	247	820		
	50 A g^{-1}	120	400		
NMC@MXene-10	1 A g^{-1}	236	790		
	50 A g^{-1}	84	280		
NMC	1 A g^{-1}	227	757		
	50 A g^{-1}	75	250		
MXene	1 A g^{-1}	230	575		
	50 A g^{-1}	63	160		
MXene/NMC	1 A g^{-1}	266	887		
	50 A g^{-1}	83	277		

curve display isosceles triangular curves at various current densities, indicating high-capacitive reversibility for the NMC@MXene-30-based supercapacitor (Fig. S17a†). The cycling stability of the NMC@MXene-30-based supercapacitor as measured by the CV test is shown in Fig. 9b. The specific capacitance retains 97.5% of its initial value after 10 000 cycles, suggesting superior cycling stability of the NMC@MXene-30 electrode. Fig. S17b† displays the C_m of the NMC@MXene-30 electrode calculated from the charge–discharge curves at different current densities. Remarkably, the NMC@MXene-30 electrode exhibits a high C_m of 210 F g^{-1} at 1 A g^{-1} and 102 F g^{-1} at 50 A g^{-1}, indicating good rate capability. Additionally, the C_v of the NMC@MXene-30 electrode was calculated to be 666 F cm^{-3} at 1 A g^{-1} and 337 F cm^{-3} at 50 A g^{-1} (Fig. S17c†). The Nyquist plots shown in Fig. S18d† indicate low ESR and low ion-diffusion resistance in the high-frequency and low-frequency regions, respectively. To further evaluate the practical application of devices comprised of the NMC@MXene-30, a comparison of Ragone plots for the NMC@MXene-30-based symmetric cell based on weight, and volume, with other previously published results, is presented in Fig. 9c. It is worth noting that the gravimetric energy density maintains a value of 8.1 W h kg^{-1} when the power density increases to 0.25 kW kg^{-1} and remains at 2.5 W h kg^{-1} at a power density of 12.75 kW kg^{-1}. These values are much higher than those reported for MXene-based symmetric supercapacitors.[19,20,34,54,65–68]

In addition, Fig. 9d shows that the volumetric energy density of the NMC@MXene-30-based cell achieves 23.13 W h L^{-1} at a power density of 0.8 kW kg^{-1} and maintains a high value of 12 W h L^{-1} at a power density of 43 kW L^{-1}. These values far exceeded those of previously reported 2D MXene and carbon-based symmetric cells.[20,65,69–74] The outstanding electrochemical behavior of the NMC@MXene-based cell is due to the unique architecture of interconnected MXene networks with assembled MC structures and large surface area which can confer more active sites for redox reactions and facilitate electrolyte ion diffusion, leading to the effective practical application of the active material.

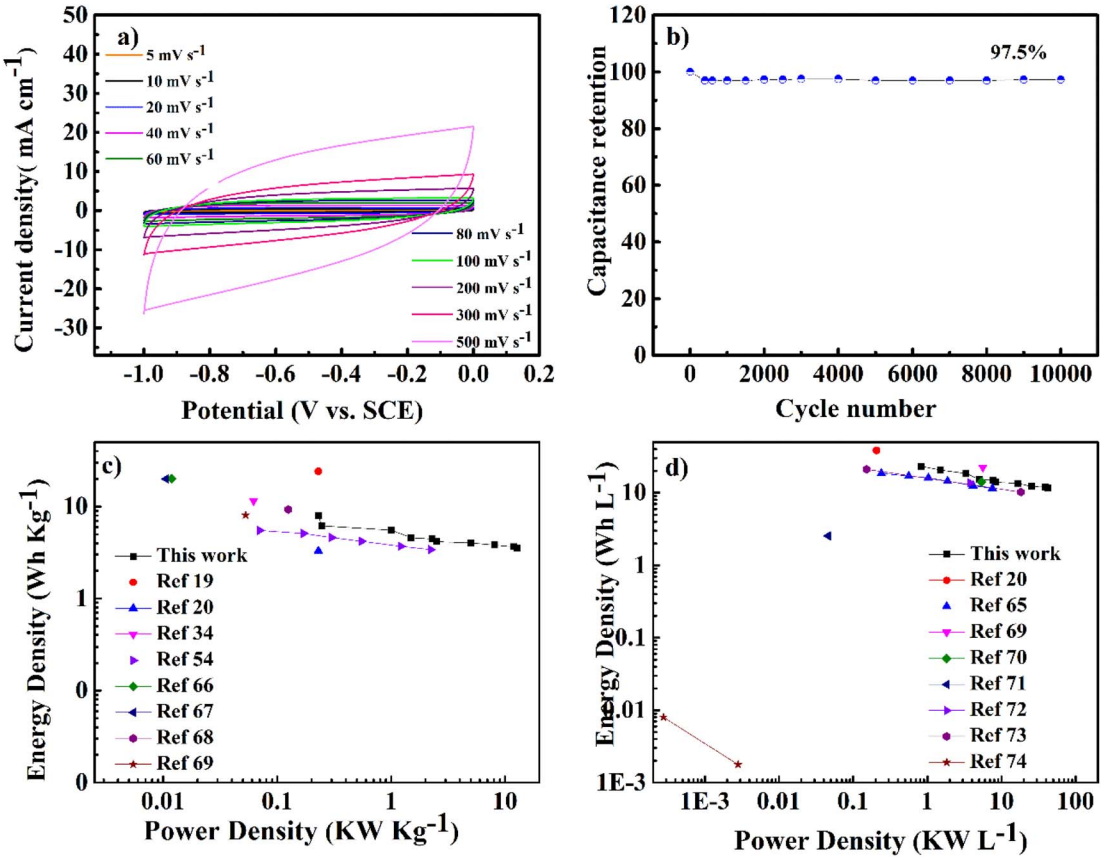

Fig. 9 Electrochemical performance of NMC@MXene-30 in a two-electrode system: (a) CV curves at various scan rates, (b) cycling stability at a scan rate of 100 mV s^{-1} and Ragone plots, (c) gravimetric energy and power densities, and (d) volumetric energy and power densities of the electrode material in comparison with previously reported materials.

4. Conclusion

In summary, I present the facile method for preparation of a 3D heterostructure with NMC between 2D MXene layers *via* interfacial self-assembly of block copolymer P123/melamine–formaldehyde resin micelles and exfoliated MXene nanosheets. NMC with onion morphology and open channels prevents the restacking of MXene layers and provides quick ion-diffusion paths. When employed for supercapacitor applications, the electrochemical behavior trend is in decreasing order: NMC@MXene-30 > NMC@MXene-20 > NMC@MXene-10 > NMC and MXene. These results indicate the benefit of extra MXene for enhancing super-capacitive performance. The NMC@MXene-30 electrode manifested both high gravimetric and volumetric capacitance, good rate capability, and excellent stability. It is expected that the simple and reliable synthesis approach proposed here will provide a simple way to design 2D heterostructured materials with eminent electrochemical properties for energy storage and conversion applications.

Conflicts of interest

There are no conflicts to declare.

References

1 L. L. Zhang and X. S. Zhao, *Chem. Soc. Rev.*, 2009, **38**, 2520–2531.
2 Y. Zhai, Y. Dou, D. Zhao, P. F. Fulvio and R. T. Mayes, *Adv. Mater.*, 2011, 4828–4850.
3 J. Cherusseri and K. K. Kar, *J. Mater. Chem. A*, 2015, 21586–21598.
4 T. Lin, I.-W. Chen, F. Liu, C. Yang, H. Bi, F. Xu and F. Huang, *Science*, 2015, **350**(6267), 1508–1513.
5 H. Li, Y. Wang, C. Wang and Y. Xia, *J. Power Sources*, 2008, **185**, 1557–1562.
6 J. Liang, X. Du, C. Gibson, X. W. Du and S. Z. Qiao, *Adv. Mater.*, 2013, 6226–6231.
7 R. Liu, L. Wan, S. Liu, L. Pan, D. Wu and D. Zhao, *Adv. Funct. Mater.*, 2015, 526–533.
8 B. Guo, X. Wang, P. F. Fulvio, M. Chi and S. M. Mahurin, *Adv. Mater.*, 2011, 1–6.
9 G. R. Bhimanapati, Z. Lin, V. Meunier, Y. Jung, J. Cha, S. Das, D. Xiao, Y. Son, X. M. S. Strano, X. V. R. Cooper, O. L. Liang, S. G. Louie, E. Ringe, W. Zhou, O. S. S. Kim, R. R. Naik, B. G. Sumpter, O. H. Terrones, F. Xia, Y. Wang, J. Zhu, D. Akinwande, N. Alem, J. A. Schuller, R. E. Schaak,

Â. M. Terrones and J. A. Robinson, *ACS Nano*, 2015, 11509–11539.
10 T. Sasaki, *Acc. Chem. Res.*, 2015, **48**(1), 136–143.
11 L. Chen, Y. Liu and Y. Zhao, *Nanotechnology*, 2016, **27**, 172001.
12 J. Gao, Y. Feng and W. Guo, *Chem. Soc. Rev.*, 2017, 5400–5424.
13 J. Jiang, Y. Zhang, P. Nie, G. Xu, M. Shi, J. Wang and Y. Wu, *Adv. Sustainable Syst.*, 2018, **1700110**, 1–24.
14 M. Naguib, M. Kurtoglu, V. Presser, J. Lu, J. Niu, M. Heon, L. Hultman, Y. Gogotsi and M. W. Barsoum, *Adv. Mater.*, 2011, **23**, 4248–4253.
15 M. R. Lukatskaya, O. Mashtalir, C. E. Ren, Y. Dall'Agnese, P. Rozier, P. L. Taberna, M. Naguib, P. Simon, M. W. Barsoum and Y. Gogotsi, *Science*, 2013, **341**(6153), 1502–1505.
16 S. Ponnada, M. S. Kiai, D. B. Gorle, R. S. C. Bose, V. Rajagopal, B. Saini, M. Kathiresan, A. Nowduri, R. Singhal, F. Marken, M. A. Kulandainathan, K. K. Nanda and R. K. Sharma, *Catal. Sci. Technol.*, 2022, **12**, 4413–4441.
17 Y. Z. Zhang, J. K. El-Demellawi, Q. Jiang, G. Ge, H. Liang, K. Lee, X. Dong and H. N. Alshareef, *Chem. Soc. Rev.*, 2020, **49**, 7229–7251.
18 S. Panda, K. Deshmukh, S. K. Khadheer Pasha, J. Theerthagiri, S. Manickam and M. Y. Choi, *Coord. Chem. Rev.*, 2022, **462**, 214518.
19 J. Yan, C. E. Ren, K. Maleski, C. B. Hatter, B. Anasori, P. Urbankowski, A. Sarycheva and Y. Gogotsi, *Adv. Funct. Mater.*, 2017, **27**, 1–10.
20 Z. Fan, Y. Wang, Z. Xie, D. Wang, Y. Yuan, H. Kang, B. Su, Z. Cheng and Y. Liu, *Adv. Sci.*, 2018, **5**(10), 1800750.
21 W. Xi, Y. Zhang, J. Zhang, R. Wang, Y. Gong, B. He, H. Wang and J. Jin, *J. Mater. Chem. C*, 2023, **11**, 2414–2429.
22 E. E. Elemike, O. E. Osafile and E. Omugbe, *J. Energy Storage*, 2021, **42**, 102993.
23 S. Ponnada, M. S. Kiai, R. Krishnapriya, R. Singhal and R. K. Sharma, *Energy Fuels*, 2022, **36**, 6013–6026.
24 S. Ponnada, D. Babu Gorle, R. S. Chandra Bose, M. Sadat Kiai, M. Devi, C. Venkateswara Raju, N. Baydogan, K. Kar Nanda, F. Marken and R. K. Sharma, *Batteries Supercaps*, 2022, **5**(8), e202200223.
25 S. Ponnada, M. S. Kiai, D. B. Gorle and A. Nowduri, *Mater. Adv.*, 2021, **2**, 4115–4139.
26 S. Ponnada, M. S. Kiai, D. B. Gorle and A. Nowduri, *Energy Fuels*, 2021, **35**, 12619–12627.
27 S. Ponnada, M. S. Kiai, D. B. Gorle and A. Nowduri, *Nanoscale Adv.*, 2021, **3**, 4492–4501.
28 Z. Liu, H. Xiong, Y. Luo, L. Zhang, K. Hu, L. Zhang, Y. Gao and Z. A. Qiao, *ChemSusChem*, 2021, **14**, 4422–4430.
29 Q. X. Xia, J. Fu, J. M. Yun, R. S. Mane and K. H. Kim, *RSC Adv.*, 2017, **7**, 11000–11011.
30 B. Ahmed, D. H. Anjum, M. N. Hedhili, Y. Gogotsi and H. N. Alshareef, *Nanoscale*, 2016, **8**, 7580–7587.
31 F. Kong, X. He, Q. Liu, X. Qi, Y. Zheng, R. Wang and Y. Bai, *Electrochim. Acta*, 2018, **265**, 140–150.
32 M. W. Barsoum, L. Hultman, J. Carle, J. Lu, O. Mashtalir, V. Presser, M. Naguib and Y. Gogotsi, *ACS Nano*, 2012, **6**, 1322–1331.
33 G. Zhu, L. Ma, H. Lv, Y. Hu, T. Chen, R. Chen, J. Liang, X. Wang, Y. Wang, C. Yan, Z. Tie, Z. Jin and J. Liu, *Nanoscale*, 2017, **9**, 1237–1243.
34 S. Wang, J. Qin, Y. Zhao, L. Duan, J. Wang, W. Gao, R. Wang, C. Wang, M. Pal, Z. S. Wu, W. Li and D. Zhao, *ChemSusChem*, 2019, **12**, 3541–3549.
35 X. Dong, Y. Zhang, B. Ding, X. Hao, H. Dou and X. Zhang, *J. Power Sources*, 2018, **390**, 208–214.
36 T. Li, B. Ding, J. Wang, Z. Qin, J. F. S. Fernando, Y. Bando, A. K. Nanjundan, Y. V. Kaneti, D. Golberg and Y. Yamauchi, *ACS Appl. Mater. Interfaces*, 2020, **12**, 14993–15001.
37 X. Wu, Z. Wang, M. Yu, L. Xiu and J. Qiu, *Adv. Mater.*, 2017, **29**, 1607017.
38 Y. Meng, D. Gu, F. Zhang, Y. Shi, L. Cheng, D. Feng, Z. Wu, Z. Chen, Y. Wan, A. Stein, D. Zhao, R. V April, V. Re, M. Recei and V. July, *Chem. Mater.*, 2006, 4447–4464.
39 W. Bao, L. Liu, C. Wang, S. Choi, D. Wang and G. Wang, *Adv. Energy Mater.*, 2018, **8**, 1–11.
40 J. Halim, K. M. Cook, M. Naguib, P. Eklund, Y. Gogotsi, J. Rosen and M. W. Barsoum, *Appl. Surf. Sci.*, 2016, **362**, 406–417.
41 L. Shen, X. Zhou, X. Zhang, Y. Zhang, Y. Liu, W. Wang, W. Si and X. Dong, *J. Mater. Chem. A*, 2018, **6**, 23513–23520.
42 T. Zhao, J. Zhang, Z. Du, Y. Liu, G. Zhou and J. Wang, *Electrochim. Acta*, 2017, **254**, 308–319.
43 X. Wu, Z. Wang, M. Yu, L. Xiu and J. Qiu, *Adv. Mater.*, 2017, **1607017**, 1–8.
44 Y. Zhang, H. Jiang, Y. Lin, H. Liu, Q. He, C. Wu, T. Duan and L. Song, *Adv. Mater. Interfaces*, 2018, **5**, 1–9.
45 I. Kusunoki, M. Sakai, Y. Igari, S. Ishidzuka and T. Takami, *Surf. Sci.*, 2001, **492**, 315–328.
46 H. M. Jeong, J. W. Lee, W. H. Shin, Y. J. Choi, H. J. Shin, J. K. Kang and J. W. Choi, *Nano Lett.*, 2011, 2472–2477.
47 Z. Sheng, L. Shao, J. Chen, W. Bao, F. Wang and X. Xia, *ACS Nano*, 2011, 4350–4358.
48 K. Wang, Y. Zhou, W. Xu, D. Huang and Z. Wang, *Ceram. Int.*, 2016, **42**, 8419–8424.
49 M. R. Lukatskaya, S. Bak, X. Yu, X. Yang and M. W. Barsoum, *Adv. Energy Mater.*, 2015, 2–5.
50 X. Wang, S. Kajiyama, H. Iinuma, E. Hosono, S. Oro, I. Moriguchi, M. Okubo and A. Yamada, *Nat. Commun.*, 2015, **6**, 1–6.
51 S. Cho, D. Y. Kim and Y. Seo, *Adv. Mater. Interfaces*, 2020, **7**, 1–8.
52 M. R. Lukatskaya, S. Kota, Z. Lin, M.-Q. Zhao, N. Shpigel, M. D. Levi, J. Halim, P.-L. Taberna, M. W. Barsoum, P. Simon and Y. Gogotsi, *Nat. Energy*, 2017, **2**, 17105.
53 H. Hwang, S. Byun, S. Yuk, S. Kim, S. H. Song and D. Lee, *Appl. Surf. Sci.*, 2021, **556**, 149710.
54 Y. Wen, T. E. Rufford, X. Chen, N. Li, M. Lyu, L. Dai and L. Wang, *Nano Energy*, 2017, **38**, 368–376.
55 A. S. Levitt, M. Alhabeb, C. B. Hatter, A. Sarycheva, G. Dion and Y. Gogotsi, *J. Mater. Chem. A*, 2019, **7**, 269–277.

56 Y. Zhou, K. Maleski, B. Anasori, J. O. Thostenson, Y. Pang, Y. Feng, K. Zeng, C. B. Parker, S. Zauscher, Y. Gogotsi, J. T. Glass and C. Cao, *ACS Nano*, 2020, **14**, 3576–3586.
57 Y. S. Kwon, J.-S. Lee, G.-H. Hwang and Y. G. Jeong, *Macromol. Mater. Eng.*, 2022, **307**, 2100877.
58 S. Xu, G. Wei, J. Li, W. Han and Y. Gogotsi, *J. Mater. Chem. A*, 2017, 17442–17451.
59 M. Q. Zhao, C. E. Ren, Z. Ling, M. R. Lukatskaya, C. Zhang, K. L. Van Aken, M. W. Barsoum and Y. Gogotsi, *Adv. Mater.*, 2015, **27**, 339–345.
60 M. Boota, B. Anasori, C. Voigt, M.-Q. Zhao, M. W. Barsoum and Y. Gogotsi, *Adv. Mater.*, 2016, **28**, 1517–1522.
61 M. Xie, H. Meng, J. Chen, Y. Zhang, C. Du, L. Wan and Y. Chen, *ACS Appl. Energy Mater.*, 2021, **4**, 1840–1850.
62 J. Gamby, P. L. Taberna, P. Simon, J. F. Fauvarque and M. Chesneau, *J. Power Sources*, 2001, **101**, 109–116.
63 A. Enaiet Allah, H. Tan, X. Xu, A. A. Farghali, M. H. Khedr, A. A. Alshehri, Y. Bando, N. A. Kumar and Y. Yamauchi, *Nanoscale*, 2018, **10**, 12398–12406.
64 C. Zequine, C. K. Ranaweera, Z. Wang, S. Singh, P. Tripathi, O. N. Srivastava, B. K. Gupta, K. Ramasamy, P. K. Kahol, P. R. Dvornic and R. K. Gupta, *Sci. Rep.*, 2016, **6**, 1–10.
65 M. R. Lukatskaya, O. Mashtalir, C. E. Ren, Y. Dall'Agnese, P. Rozier, P. L. Taberna, M. Naguib, P. Simon, M. W. Barsoum and Y. Gogotsi, *Science*, 2013, **341**, 1502–1505.
66 Y. Yoon, M. Lee, S. K. Kim, G. Bae, W. Song, S. Myung, J. Lim, S. S. Lee, T. Zyung and K. S. An, *Adv. Energy Mater.*, 2018, **8**, 1–11.
67 J. K. Guo, J. Liu and L. Bin Kong, *ChemElectroChem*, 2020, **7**, 2592–2598.
68 M. Yao, Y. Chen, Z. Wang, C. Shao, J. Dong, Q. Zhang, L. Zhang and X. Zhao, *Chem. Eng. J.*, 2020, **395**, 124057.
69 X. Dong, N. Hu, L. Wei, Y. Su, H. Wei, L. Yao, X. Li and Y. Zhang, *J. Mater. Chem. A*, 2016, **4**, 9739–9743.
70 C. Yang, Y. Tang, Y. Tian, Y. Luo, Y. He, X. Yin and W. Que, *Adv. Funct. Mater.*, 2018, **28**, 1–11.
71 C. Yu, Y. Gong, R. Chen, M. Zhang, J. Zhou, J. An, F. Lv, S. Guo and G. Sun, *Small*, 2018, **14**, 1–7.
72 Y. Tian, C. Yang, W. Que, X. Liu, X. Yin and L. B. Kong, *J. Power Sources*, 2017, **359**, 332–339.
73 Y. Tian, W. Que, Y. Luo, C. Yang, X. Yin and L. B. Kong, *J. Mater. Chem. A*, 2019, **7**, 5416–5425.
74 Z. Guo, Y. Li, Z. Lu, Y. Chao and W. Liu, *J. Mater. Sci.*, 2022, **57**, 3613–3628.